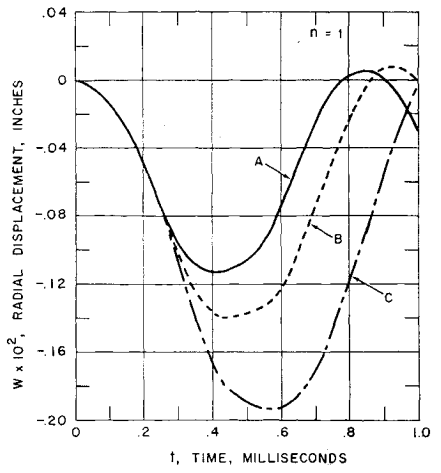

Fig. 3 Comparison of dynamic displacement histories for $n = 1$ at midspan of a cylinder with clamped boundaries. A) isotropic, B) ¾ isotropic shear modulus, C) ½ isotropic shear modulus.

the calculated points have been connected by straight lines to illustrate the trends.

It is of interest to note that, as harmonic number is increased past $n = 4$, the radial displacement ratios for $\delta > 0$ approach those for $\delta < 0$ and both appear to approach a horizontal tangent. This result is not immediately obvious from an examination of the coefficients of Eqs. (5) of Ref. 1. Similar calculations were performed for the same cylinder in which the values of E_1 and E_2 were interchanged and again E_2 was varied with essentially the same results. One pronounced difference in the cases studied was a maximum displacement difference occurring at $n = 4$ in the latter cases for $\delta > 0$ rather than at $n = 3$, as shown in Fig. 1. This result is not at all unlikely in practical situations involving composite layers in shells.

Nonzero values of $C_{12}^{(1)}$ and $G^{(1)}$ as well as variations in boundary conditions also produced similar effects. Nondimensional displacement profiles for the clamped-free cylinder subjected to a load $q = -\cos 3\theta$ are shown in Fig. 2. Coupling parameter values of $\delta = \pm\frac{1}{2}$ for both $C_{12}^{(1)}$ and $C_2^{(1)}$ variations, as well as the uncoupled case, $\delta = 0$, are presented. Note that increasing the circumferential stiffness in the inner layer while reducing it in the outer layer (i.e., $\delta = \frac{1}{2}$ for $C_2^{(1)}$) produces a displacement profile similar to the case where both the axial and circumferential Poisson's ratios are increased in the outer layer while being reduced in the inner layer (i.e., $\delta = -\frac{1}{2}$ for $C_{12}^{(1)}$). The major difference is that the latter produces displacements relatively close to the uncoupled results whereas the former produces displacements about 20–30% larger.

The similarity in the profiles for opposite signs in δ gives an indication of how Poisson's ratio is related to the direct stiffness. Increasing Poisson's ratio in one layer is, in some respects, equivalent to reducing the circumferential stiffness in the same layer. An additional effect involving Poisson's ratio is noted from an examination of an axisymmetric normal load on a free-free two-layer cylinder. If the Poisson's ratios are the same in both layers, the axial moment m_ξ will be identically zero over the length of the cylinder, whereas if coupling of the Poisson ratio terms is introduced, an axial moment will exist along the length of the cylinder with the exception of the free ends. This result is not restricted to orthotropic materials, but will also appear for isotropic layers since it is apparently a consequence of the Kirchoff hypothesis, which requires the cross section to remain plane. The Poisson coupling tends to distort the cross section and is restrained from doing so by the axial moment.

In another example it was of interest to evaluate the effects of "reduced" shear modulus in composite materials, which in most cases is considerably lower than the corresponding isotropic shear modulus $E_{12} = E/2(1 + \nu)$. A cylinder, clamped at both ends ($s = 0, \bar{s}$: $U_\xi = U_\theta = W = \Phi_\xi = 0$) and subjected to a normal triangular blast loading $q = -g(t)\cos n\theta$, is studied. Here,

$$g(t) = \begin{cases} (0.25 \times 10^6)t, & t \leq 4 \times 10^{-6} \\ (0.01 - t)/0.009996, & 4 \times 10^{-6} \leq t \leq 10^{-2} \\ 0, & t \geq 10^{-2} \end{cases}$$

The geometry and material properties are $r = 10$ in., $L = 60$ in., $h = \frac{1}{4}$ in., $\bar{\rho} = 0.2 \times 10^{-4}$ lb sec²/in.³, $E_1/(1 - \nu_1\nu_2) = E_2/(1 - \nu_1\nu_2) = 10^7$ psi, $\nu_1 = \nu_2 = 0.15$, and three values of the shear modulus: A) $E_{12} = 0.425 \times 10^7$ psi (isotropic), B) $E_{12} = 0.31875 \times 10^7$ psi, and C) $E_{12} = 0.2125 \times 10^7$ psi.

The normal displacement response for the $n = 1$ harmonic is shown for the midspan location in Fig. 3 and, as expected, the frequency is decreasing with shear modulus since this corresponds to an over-all reduction in stiffness of the structure. It is of interest to note that a 50% reduction in shear modulus (case C) produces almost twice the maximum deflection of the isotropic case A.

It is apparent that omission of the coupling coefficients [$\mu = 1$ in Eqs. (3), Ref. 1] can lead to important errors in the solution of multilayer shell problems. Although the numerical results were presented for cylindrical shells, it appears evident, from an investigation of the coefficients of Eqs. (5) of Ref. 1, that for general shells of revolution omission of the coupling terms can similarly lead to large errors. The use of isotropic theories for materials whose properties differ from isotropic by virtue of a "reduced" shear modulus can, as evidenced by the last example, also be erroneous. The present results are an initial effort to evaluate some effects of material coupling, and although the results cannot be stated in general terms, they indicate a need for further study.

References

[1] Tene, Y., "Deformation of Asymmetrically Loaded, Symmetrically Prestressed Orthotropic Shells of Revolution," *AIAA Journal*, Vol. 6, No. 8, Aug. 1968, pp. 1599–1602.

[2] Budiansky, B. and Radkowski, P. P., "Numerical Analysis of Unsymmetrical Bending of Shells of Revolution," *AIAA Journal*, Vol. 1, No. 8, Aug. 1963, pp. 1833–1842.

[3] Rossettos, J. N. and Tene, Y., "Analysis of Prestressed Layered Shells with Applications to Buckling," *AIAA Journal*, Vol. 5, No. 9, Sept. 1967, pp. 1720–1722.

[4] Johnson, D. E. and Greif, R., "Dynamic Response of a Cylindrical Shell: Two Numerical Methods," *AIAA Journal*, Vol. 4, No. 3, March 1966, pp. 486–494.

Response Characteristics of Thin Foil Heat Flux Sensors

ROBERT L. ASH*
Old Dominion University, Norfolk, Va.

Introduction

THE asymptotic or Gardon type heat flux transducer has become increasingly important in the aerospace industry. Among the advantages of this type of transducer are direct readout and rapid response to time varying heat fluxes.

Received March 19, 1969; revision received August 8, 1969. The author wishes to thank Robert A. Babcock and Robert E. Wright at NASA Langley Field, Va. for bringing this problem to his attention.

* Assistant Professor of Engineering. Member AIAA.

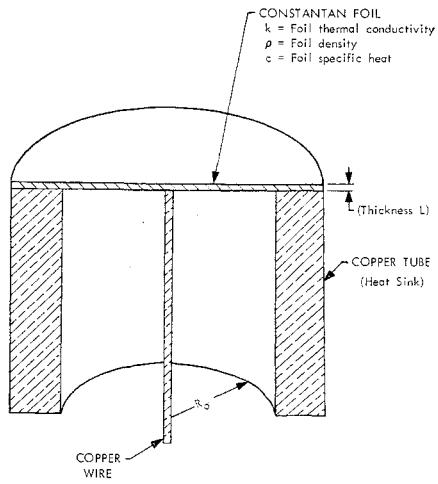

Fig. 1 Sketch of the heat flux sensor.

This rapid response behavior has been demonstrated in the laboratory, but has not been shown with a mathematically based theory. The purpose of this paper is to present such an analysis.

Little theoretical literature has been presented on this type of transducer. Robert Gardon's[1] original work explained the theory of operation and developed design criteria. Malone[2] investigated the steady-state temperature distribution in the foil for a convective environment and determined the effect of the center-line wire on the temperature distribution. Finally, Woodruff, Hearne, and Keliher[3] have investigated errors produced in the readout due to thermal disruption of the boundary layer.

Theory

A cross section of the sensor under study is shown in Fig. 1 along with appropriate dimensions and properties. Neglecting temperature variations through the foil thickness and assuming constant thermal properties, an energy balance yields

$$\rho c \partial T/\partial t = (k/r)(\partial/\partial r)(r\partial T/\partial r) + q''(t)/L \quad (1)$$

Assuming variations in the heat sink temperature are negligible and taking that temperature as the zero reference, the boundary conditions are

$$T(r,0) = T(R_0,t) = (\partial T/\partial r)(0,t) = 0 \quad (2)$$

The analyses of two general cases follow. These results can be extended to more general problems by the use of Duhamel integrals when the heat flux varies, or by using Kirchhoff's transformation for variable thermal conductivity in radiatively heated devices.

Case 1: A suddenly applied, constant heat flux

In this case, $q''(t) = q_0 = \text{const}$, for $t > 0$. Consequently, the governing equation becomes

$$\partial T/\partial t = (\alpha/r)(\partial/\partial r)(r\partial T/\partial r) + q_0/\rho cL \quad (3)$$

where α is the thermal diffusivity. By defining a new variable $\theta(r,t)$, given by

$$\theta(r,t) = T(r,t) - (R_0^2 q_0/4kL)[1 - (r/R_0)^2] \quad (4)$$

the governing equation is made homogeneous and the new boundary conditions are

$$\theta(R_0,t) = (\partial\theta/\partial r)(0,t) = 0 \quad (5)$$

and

$$\theta(r,0) = (q_0 R_0^2/4kL)[(r/R_0)^2 - 1] = \phi(r) \quad (6)$$

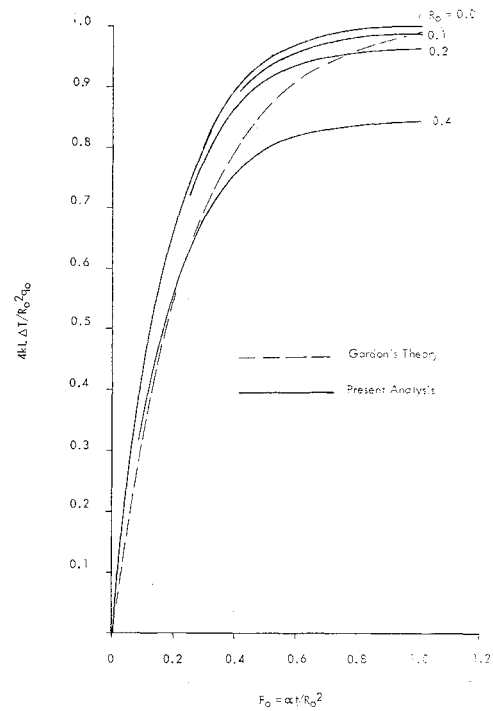

Fig. 2 Dimensionless temperature difference vs Fourier number for a suddenly applied, constant heat flux.

Using separation of variables, the solution to this equation is

$$\theta(r,t) = \sum_{n=1}^{\infty} a_n e^{-\alpha\lambda_n^2 t} J_0(\lambda_n r) \quad (7)$$

where the λ_n's are roots of $J_0(\lambda_n R_0) = 0$, and the a_n's are given by

$$a_n = \frac{\int_0^{R_0} r\phi(r) J_0(\lambda_n r) dr}{\int_0^{R_0} r J_0^2(\lambda_n r) dr} = \frac{q_0 J_2(\lambda_n R_0)}{kL\lambda_n^2 J_1^2(\lambda_n R_0)} \quad (8)$$

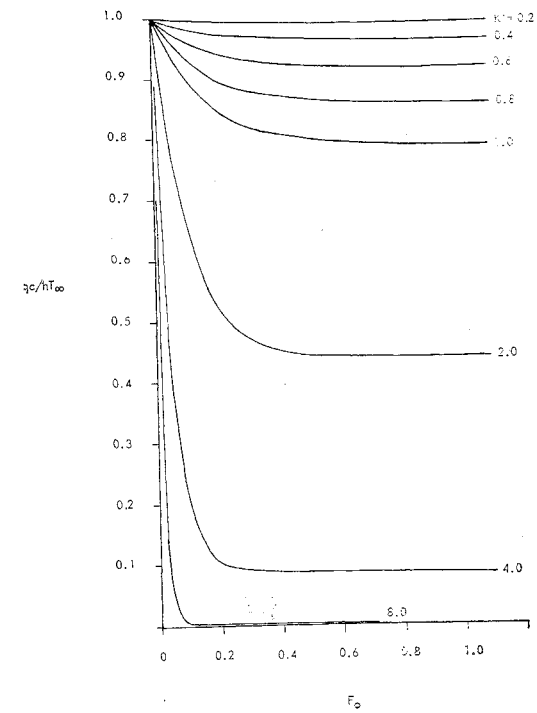

Fig. 3 Dimensionless centerline heat flux vs Fourier number when the sensor is suddenly exposed to a constant temperature convective environment.

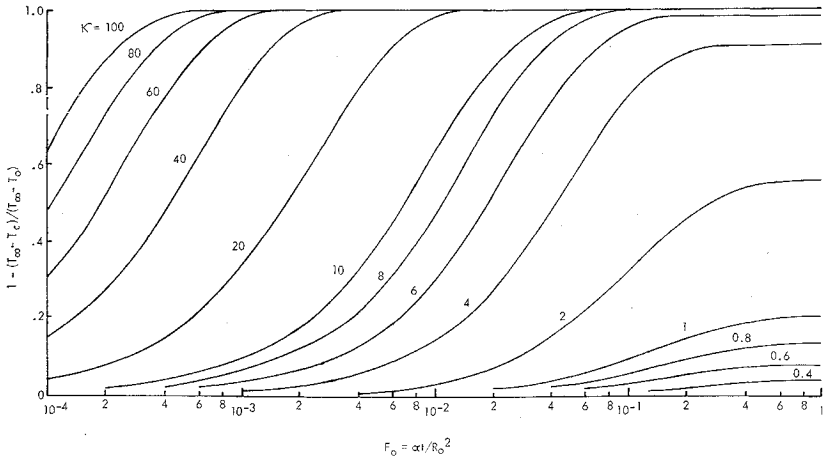

Fig. 4 Dimensionless temperature response to the convective environment for different values of κ.

Or, letting $\gamma_n = \lambda_n R_0$, and writing in terms of $T(r,t)$

$$T(r,t) = \frac{q_0 R_0^2}{4kL}\left[1 - \left(\frac{r}{R_0}\right)^2 - 4\sum_{n=1}^{\infty}\frac{J_2(\gamma_n)J_0(\gamma_n r/R_0)}{\gamma_n^2 J_1^2(\gamma_n)} \times e^{-\alpha\gamma_n^2 t/R_0^2}\right] \quad (9)$$

Defining $\Delta T(t)$ as the instantaneous temperature difference between the foil centerline and the foil-heat sink interface, the dimensionless indicated temperature difference can be written

$$\frac{4kL\Delta T(t)}{q_0 R_0^2} = 1 - 8\sum_{n=1}^{\infty}\frac{e^{-\gamma_n^2 F_0}}{\gamma_n^3 J_1(\gamma_n)} \quad (10)$$

where F_0 is the Fourier number ($\alpha t/R_0^2$). The denominator has been simplified by making use of the identity $J_2(\gamma_n) = (2/\gamma_n)J_1(\gamma_n) - J_0(\gamma_n) = (2/\gamma_n)J_1(\gamma_n)$.

The response of the foil to a step function heat input is shown in Fig. 2. The response predicted by the present theory is compared to the exponential equation originally used by Gardon in his approximation for the sensor response. In addition, Eq. (9) has been used to show the effects of errors in location of the center-line thermocouple wire on the sensor output. Parameter (r/R_0) represents the fractional error.

Case II: Sudden exposure to a convective environment

Assuming the reference temperature, T_∞, and the heat-transfer coefficient, h, are constant, the governing equation is

$$\partial T/\partial t = (\alpha/r)(\partial/\partial r)(r\partial T/\partial r) + (h/\rho cL)[T_\infty - T(r,t)] \quad (11)$$

The boundary conditions are the same as those given in Eq. (2). As before, a new variable $\theta(r,t)$ can be defined which makes the governing equation homogeneous. That is,

$$\theta(r,t) = T(r,t) - T_\infty\left\{1 - \frac{I_0[(h/kL)^{1/2}r]}{I_0[(h/kL)^{1/2}R_0]}\right\} \quad (12)$$

with boundary conditions

$$\theta(R_0,t) = (\partial\theta/\partial r)(0,t) = 0 \quad (13)$$

and

$$\theta(r,0) = T_\infty\left\{\frac{I_0[(h/kL)^{1/2}r]}{I_0[(h/kL)^{1/2}R_0]} - 1\right\} = \phi(r) \quad (14)$$

Again, using separation of variables, the solution has the form

$$\theta(r,t) = \sum_{n=1}^{\infty} a_n \exp[-\{(h/\rho cL) + \lambda_n^2\alpha\}t]\, J_0(\lambda_n r) \quad (15)$$

where

$$a_n = \frac{-2T_\infty}{\lambda_n R_0 J_1(\lambda_n R_0)}\left[\frac{hR_0^2/kL}{\lambda_n^2 R_0^2 + (hR_0^2/kL)}\right] \quad (16)$$

Hence, rearranging

$$\frac{[T_\infty - T(r,t)]}{T_\infty} = \frac{I_0[(h/kL)^{1/2}r]}{I_0[(h/kL)^{1/2}/R_0]} + \left(\frac{2hR_0^2}{kL}\right)\cdot \sum_{n=1}^{\infty} \times \frac{e^{[-(\alpha/R_0^2)\{(hR_0^2/kL) + \lambda_n^2 R_0^2\}t]}\, J_0(\lambda_n r)}{\lambda_n R_0 J_1(\lambda_n R_0)[\lambda_n^2 R_0^2 + (hR_0^2/kL)]} \quad (17)$$

Making use of the dimensionless Fourier number, Biot number (B_i), aspect ratio (A), and defining a dimensionless eigenvalue (γ_n), and response constant (κ), where

$$B_i = 2hR_0/k;\quad A = 2R_0/L;\quad \gamma_n = \lambda_n R_0$$
$$\kappa = (AB_i/4)^{1/2} \quad (18)$$

the solution can be written

$$\frac{T_\infty - T(\zeta,F_0)}{T_\infty} = \frac{I_0(\kappa\zeta)}{I_0(\kappa)} + 2\kappa^2\sum_{n=1}^{\infty}\frac{e^{-\{\kappa^2 + \gamma_n^2\}F_0}\, J_0(\gamma_n\zeta)}{J_1(\gamma_n)\gamma_n(\gamma_n^2 + \kappa^2)} \quad (19)$$

where $\zeta = r/R_0$.

Realizing $[T_\infty - T(0,F_0)]/T_\infty = q_c(F_0)/hT_\infty$, where $q_c(F_0)$ represents the heat flux through the foil center-line, which is a function only of time, we can write

$$\frac{q_c(F_0,\kappa)}{hT_\infty} = \frac{1}{I_0(\kappa)} + 2\kappa^2\sum_{n=1}^{\infty}\frac{e^{-\{\kappa^2 + \gamma_n^2\}F_0}}{\gamma_n\{\gamma_n^2 + \kappa^2\}J_1(\gamma_n)} \quad (20)$$

The response of the foil to a convective environment is shown in Figs. 3 and 4 for various values of κ. Figure 3 shows the measured centerline heat flux as a function of time for different values of κ. It should be noted that T_c is the temperature at the foil center-line. In addition, since the heat sink temperature is actually nonzero, it has been designated T_0 in Fig. 4.

Conclusions

It has been shown that the theoretical response predicted for a thin foil gage when suddenly exposed to a constant heat flux agrees closely with the experimentally based response curve developed by Gardon. Furthermore, the analysis has shown that the magnitude of the heat-transfer coefficient, through response function κ, affects the response time of the sensor, as well as its response curve. This last result can perhaps be used to simultaneously obtain qualitative estimates of the heat-transfer coefficient and the appropriate reference temperature in an experimental facility.

References

[1] Gardon, R., "An Instrument for the Direct Measurement of Thermal Radiation," *Review of Scientific Instruments*, Vol. 24, May 1953, pp. 366–370.

[2] Malone, E. W., "Design and Calibration of Thin Foil Heat Flux Sensors," Paper P6-2-PHYMMID-67, 1967, Instrument Society of America.

[3] Woodruff, L. W., Hearne, L. F., and Keliher, T. J., "Interpretation of Asymptotic Calorimeter Measurements," *AIAA Journal*, Vol. 5, No. 4, April 1967, pp. 795–797.

Stability and Shape of Magnetically Balanced Cross-Flow Arcs

DAVID M. BENENSON* AND ALLEN J. BAKER†
State University of New York at Buffalo, Buffalo, N.Y.

EXPERIMENTAL investigations of the magnetically balanced cross-flow arcs have been reported in Refs. 1 and 2. In Ref. 1, the arc (about 5-in. length) was drawn between a thoriated tungsten cathode and a copper, coil-type anode; the electrodes were placed outside the test section. Instability occurred at speeds of about 60 ft/sec. Generally, the instability was associated with erratic behavior at the anode attachment, resulting in electrode failure (Ref. 3). Tests reported in Ref. 2 were conducted upon rail and pointed electrode configurations (electrode spacing in each case was $\frac{1}{2}$ in.); all electrodes were copper. Arc instability was followed by extinction of the arc (Ref. 4). For the pointed electrodes configuration, instability was reached at about 50 ft/sec; with rail electrodes, instability occurred at about 130 ft/sec. For both Refs. 1 and 2, visual observation of the arc was generally confined to views transverse (i.e., normal, $\alpha = 0°$) to the flow (and arc) and from the downstream direction ($\alpha = 90°$). The ratio $\bar{L}$ (characteristic dimension transverse to the flow to that in the direction of flow) was found to be of the order 1–2 (Ref. 1). This ratio was probably about the same for the rail electrode configuration of Ref. 1, even though the plasma was bulbous near one of the electrodes; comparable information for the pointed electrode configuration was not reported.

Our experience with similar plasma configurations suggests that the occurrence of such instabilities or of arc oscillations under supposedly steady-state operation (Ref. 5) may depend upon many factors (additional to velocity and arc current), including the electrode configuration, electrode material, and tunnel geometry.

Reported herein are results of tests conducted upon magnetically balanced, atmospheric, cross-flow arcs in argon. Electrodes of the pointed type were used: 90° conical tip, 0.250-in.-base-diam copper anode and a 0.080-in.-diam, 0.469-in.-long tantalum cathode. The arrangement was placed inside a $1\frac{7}{8}$-in. × $1\frac{7}{8}$-in. test section; electrode spacings were in the range $\frac{1}{4}$–$\frac{1}{2}$ in. Arc currents up to 150 amp were employed. Transverse magnetic field, uniform to within ±0.15% in a 1-in.[3] volume centered about the electrode centerline and duct centerline, was applied using a coil arrangement; field strengths in excess of 500 gauss were developed. The field arrangement permitted observation of the plasma over a wide range of azimuthal angles [with such an arrangement, the temperature distribution within the plasma will be obtained employing techniques previously developed for nonmagnetically balanced cross-flow arcs (Refs. 6, 7)].

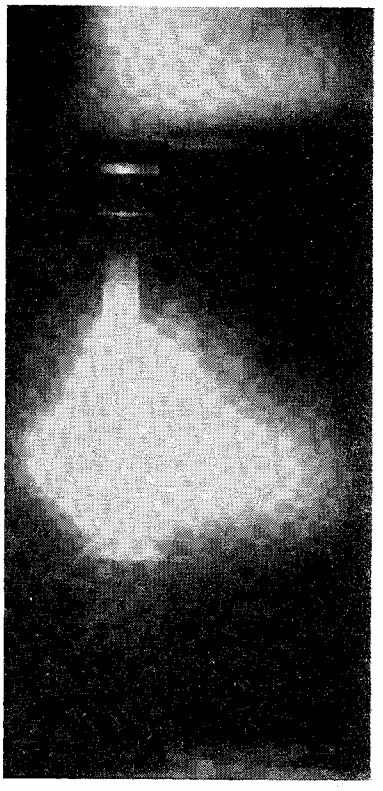

Fig. 1 Arch attachments on downstream side of electrodes: cathode over anode; $\alpha = 45°$, $U = 10.4$ fps, $I = 132$ amp, electrode spacing = 0.500 in., and $B = 18$ gauss.

Tests were carried out to velocities of about 81.5 ft/sec. Instability did not occur. Fluctuation of the central portion of the column became more pronounced at the higher velocities; the amplitude of the fluctuations was of the order of the arc dimension in the direction of flow. In all tests both anode and cathode attachment appeared fixed, i.e., steady-in position.

Two different types of balanced arc modes have been found, the configurations observed depending upon whether the plasma attachments were on the upstream or the downstream (or at the apex) side of the electrode. In turn, the location of the attachment points depended upon the velocity as well as upon the strength of the transverse magnetic field (i.e., the $\bar{J} \times \bar{B}$ body force). In fact, a critical or threshold velocity was found, below which the magnetic field available was not sufficient to force the attachment points onto the upstream side of the electrodes. Below this critical velocity, the magnetic field appeared to affect primarily the arc column. With sufficient field, the column was forced relatively far upstream; under these conditions, the plasma appeared distinctly filamentary.

As expected, for a given current and velocity, the arc may be operated in a stable mode over a wide range of magnetic fields. Under these conditions, a configuration is obtained which generally is no longer colinear (or nearly colinear) with the electrodes (i.e., no longer balanced); the resulting cusp-shaped appearance is similar to that studied previously for nonmagnetically balanced cross-flow plasmas.[6,7]

With balanced operation and with the arc attachments at the apex or on the downstream side of the electrodes, $\bar{L}$ was generally relatively large, of the order of 3–5 [Fig. 1; all photographs were taken using a narrow band (10 Å) optical interference filter centered at 4454 Å.] In comparison, plasma attachments on the upstream side of the electrode resulted in a relatively longer plasma in which the characteristic transverse dimension was of the same magnitude as the characteristic axial dimension ($\bar{L} \sim 1$–2; Figs. 2, 3).

Received April 30, 1969. This research was supported by the National Science Foundation Grant GK-1174.

* Professor, Faculty of Engineering and Applied Sciences. Associate Fellow AIAA.

† Instructor, Faculty of Engineering and Applied Sciences.